Observation of bulk states and spin-polarized topological surface states in transition metal dichalcogenide Dirac semimetal candidate $NiTe_2$

Barun Ghosh,[1] Debashis Mondal,[2,3] Chia-Nung Kuo,[4] Chin Shan Lue,[4] Jayita Nayak,[1] Jun Fujii,[2] Ivana Vobornik,[2,*] Antonio Politano,[5,6,†] and Amit Agarwal[1,‡]

[1]*Department of Physics, Indian Institute of Technology - Kanpur, Kanpur 208016, India*

[2]*Istituto Officina dei Materiali (IOM)-CNR, Laboratorio TASC, in Area Science Park, S.S.14, Km 163.5, I-34149 Trieste, Italy*

[3]*International Centre for Theoretical Physics (ICTP), Strada Costiera 11, I-34100 Trieste, Italy*

[4]*Department of Physics, National Cheng Kung University, 1 Ta-Hsueh Road 70101 Tainan, Taiwan*

[5]*Dipartimento di Scienze Fisiche e Chimiche (DSFC), Università dell'Aquila, Via Vetoio 10, I-67100 L'Aquila, Italy*

[6]*CNR-IMM Istituto per la Microelettronica e Microsistemi, VIII strada 5, I-95121 Catania, Italy*

(Received 14 August 2019; published 20 November 2019)

We predict $NiTe_2$ to be a type-II Dirac semimetal based on *ab initio* calculations and explore its bulk and spin-polarized surface states using spin- and angle-resolved photoemission spectroscopy (spin-ARPES). Our results show that, unlike $PtTe_2$, $PtSe_2$, and $PdTe_2$, the Dirac node in $NiTe_2$ is located in close vicinity to the Fermi energy. Additionally, $NiTe_2$ also hosts a pair of band inversions below the Fermi level along the Γ-A high-symmetry direction, with one of them leading to a Dirac cone in the surface states. The bulk Dirac nodes and the ladder of band inversions in $NiTe_2$ support unique topological surface states with chiral spin texture over a wide range of energies. Our work paves the way for the exploitation of the low-energy type-II Dirac fermions in $NiTe_2$ in the fields of spintronics, infrared plasmonics, and ultrafast optoelectronics.

DOI: 10.1103/PhysRevB.100.195134

I. INTRODUCTION

The discovery of topological semimetals has ushered in a new era of exploration of massless relativistic quasiparticles in crystalline solids [1–5]. These arise as emergent quasiparticles in crystals with linearly dispersing bands in the vicinity of a degenerate band crossing point (either accidental or symmetry-enforced) and are protected by crystalline symmetries [6]. Double, triple, and quadruple degeneracy of the band crossing leads to topologically protected Weyl [7–15], triple point [16–22], and Dirac fermions [23–31], respectively. In contrast to their high energy counterparts, these emergent quasiparticles are not protected by Lorentz symmetry and can also occur in a tilted form, giving rise to type-I and type-II Dirac fermions. Specifically, Na_3Bi [27,30] and Cd_3As_2 [26,31] are type-I Dirac semimetals (DSMs), while the transition metal dichalcogenides (TMDs) $PtTe_2$ [32–34], $PtSe_2$ [35], and $PdTe_2$ [33,36,37] are type-II DSM.

In group X Pd- and Pt-based dichalcogenides, the bulk Dirac node lies deep below the Fermi level ($\sim$0.6, $\sim$0.8, and $\sim$1.2 eV in $PdTe_2$, $PtTe_2$, and $PtSe_2$, respectively) [32,33,33–37], hindering their successful exploitation in technology. In contrast, $NiTe_2$ is expected to host type-II Dirac fermions in the vicinity of the Fermi energy [38]. The so far performed experimental studies on $NiTe_2$ have primarily focused on its crystal structure and transport properties while its topological band structure remains unexplored [38–45]. Motivated by this, we explored the electronic band structure of $NiTe_2$ by means of spin- and angle-resolved photoemission spectroscopy (ARPES) in combination with density functional theory (DFT).

Our *ab initio* calculations and ARPES data demonstrate the existence of a pair of type-II Dirac nodes in $NiTe_2$ along the C_3 rotation axis, lying just above the Fermi energy. Additionally, we show that $NiTe_2$ also hosts a series of inverted band gaps (IBG). Especially, one of the IBG below the Fermi level supports a Dirac cone in the surface states. Together, the bulk Dirac node and the pair of IBG in $NiTe_2$ give rise to topological spin-polarized surface states over a wide range of energies, which we explored using spin-resolved ARPES measurements. This nontrivial band morphology in $NiTe_2$ originates primarily from the $5p$-orbital manifold of the Te atoms modified by the intralayer hybridization, trigonal crystal field splitting, and spin-orbit coupling.

II. STRUCTURAL CHARACTERIZATION AND METHODOLOGY

Bulk $NiTe_2$ crystallizes in the CdI_2 type trigonal structure (space group $P\bar{3}m1$, number 164). It has a layered structure with individual monolayer stacked together via weak van der Walls force. As shown in Figs. 1(a) and 1(b), each monolayer has three sublayers, with the central Ni layer being sandwiched between two adjacent Te layers (Ni-Te bond length 2.60 Å). The observation of sharp spots in the low-energy diffraction pattern (LEED) in Fig. 1(c) confirms

*ivana.vobornik@elettra.trieste.it
†antonio.politano@iit.it
‡amitag@iitk.ac.in

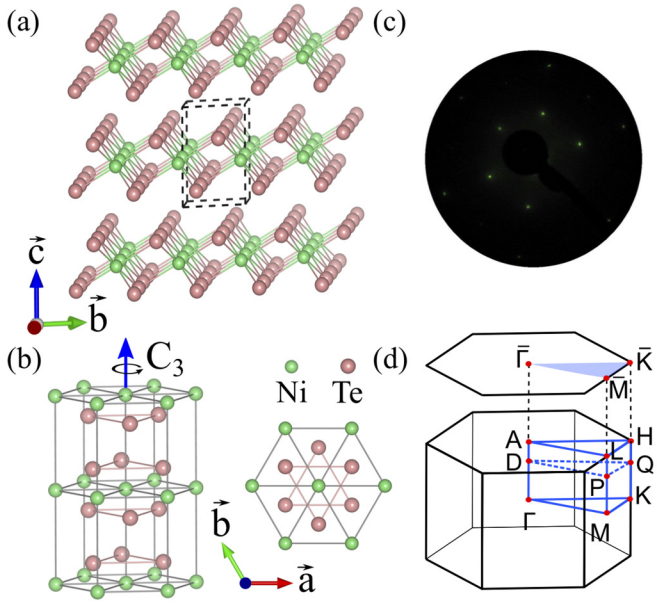

FIG. 1. (a) The side view and (b) hexagonal crystal structure of $NiTe_2$ with the C_3 rotation axis. Layers of Ni are stuffed between two Te layers. (c) The LEED pattern of (0001)-oriented $NiTe_2$ single crystals, acquired at a primary electron beam energy of 84 eV, clearly indicates its purity and the threefold symmetry along the (001) direction. (d) The bulk and the (001) surface Brillouin zone (BZ) of $NiTe_2$.

the high quality of the $NiTe_2$ crystals cleaved along the (001) direction, along with the presence of threefold symmetry. Surface cleanliness of the as-cleaved samples was checked by high-resolution electron energy loss spectroscopy and x-ray photoelectron spectroscopy. The details of crystal preparation and characterization, ARPES measurements, and DFT calculations are presented in Secs. S1, S2, and S3 of the Supplemental Material (SM) [46].

III. ELECTRONIC BAND STRUCTURE

The electronic band structure of $NiTe_2$ including spin-orbit coupling is shown in Fig. 2(a). It clearly depicts the presence of a pair of tilted band crossings along the Γ-*A* direction. The presence of inversion and time-reversal symmetry mandates these bands to be doubly degenerate. Furthermore, the Γ-*A* high-symmetry direction is the invariant subspace of the threefold rotation (C_3) symmetry, and a symmetry analysis reveals that the crossing bands have opposite rotation character. This prevents their hybridization, resulting in a pair of gapless quadruply degenerate type-II Dirac points. The type-II nature of the DSM phase is also confirmed by the fact that the Dirac point appears at the touching point of the electron and hole pocket, as highlighted in Fig. 2(b).

Our photon-energy dependent ARPES data, in part presented in Figs. 2(d) and 2(h), results in the k_z dispersion presented in Fig. 2(c). Our experimental results are consistent with the DFT-based bulk band structure calculations. Extrapolating the fitted DFT band structure, we find that the Dirac cone is located just above (∼20 meV) the Fermi energy. Our attempt to electronically dope the sample via alkali metal (potassium) deposition (see Fig. S6 in SM [46]), and shift the Fermi energy above the Dirac point, revealed that only the surface states in $NiTe_2$ are impacted by surface deposition. Bulk doing is needed to shift the bulk bands. Note that in the inset of Fig. 2(c), the photoemission measurement is unable to sufficiently resolve the lower velocity band of the Dirac node. The photoemission intensity is a product of the spectral function and the photoemission matrix elements. The low photoemission intensity of the low velocity band likely arises from the small value of the corresponding photoemission matrix element. Furthermore, the low resolution along the k_z direction is a well known shortcoming of ARPES [47].

Extended energy range ARPES spectra for the two high-symmetry directions are shown in Figs. 3(c) and 3(d). These spectra are mainly dominated by the surface states, as seen from the comparison with the calculated band structure in Figs. 3(e) and 3(f). In order to understand their origin, we note that there are two symmetry inequivalent Te atoms (Te^1 and Te^2) and a single Ni atom in a unit cell of $NiTe_2$. The electronic configuration of Ni is $4s^2 3d^8$ and that of Te is $4d^{10} 5p^4$. We find that similar to other group-X TMDs [33,48], the Te $5p$ orbital manifold in $NiTe_2$, aided by the interplay between intralayer hopping, crystal field splitting, and SOC strength, gives rise to most of the bulk Dirac nodes and multiple inverted band gaps. To highlight this, we show the evolution of the p-orbital manifold of the Te atoms in Fig. 3(a). To start with [step I in Fig. 3(a)], strong intralayer hybridization between the Te^1 and Te^2 p orbitals results in bonding and antibonding states. These orbitals are further split (in step II), due to a strong trigonal crystal field generated by the layered crystal structure of $NiTe_2$, separating p_z from the p_x, p_y orbitals. Inclusion of SOC (step III) further splits the orbitals into $|J, |m_J|\rangle$ states. Step IV of Fig. 3(a) highlights the effect of the dispersion along the Γ-*A* direction and the formation of the bulk type-II Dirac point along with multiple band inversions in the valance band.

The irreducible representation of some of these states at the Γ and *A* points and along the Γ-*A* high-symmetry line is shown in Fig. 3(b). The bulk Dirac point originates from the crossing of the Δ_4 and $\Delta_{5,6}$ states along the Γ-*A* direction. As discussed earlier, the doubly degenerate Δ_4 and $\Delta_{5,6}$ bands have opposite rotation characters (+1 and −1, respectively) and, therefore, the Dirac point is protected from gap opening by any perturbation which respects the C_3 symmetry. Additionally, Fig. 3(b) also highlights the existence of a pair of IBGs in the valance band at the *A* point. However, in comparison to $PdTe_2$, the parity of the crossing bands at the *A* point for $NiTe_2$ is different and only the lower IBG supports a Dirac node in the surface states. See Sec. S5 in the SM [46] for a more detailed discussion and comparison of the topological band structure and surface states with $PdTe_2$.

The Dirac-like conical crossing in the surface states of $NiTe_2$ (at−1.4 eV) is evident in the ARPES data taken along the two high-symmetry directions $\bar{K}$-$\bar{\Gamma}$-$\bar{K}$ and $\bar{M}$-$\bar{\Gamma}$-$\bar{M}$ as shown in Figs. 3(c) and 3(d). The dominant surface bands are indicated by the red arrows. In addition to the Dirac cone, several other surface states are present in $NiTe_2$, owing to several band inversions below and above the Fermi level. Along the $\bar{M}$-$\bar{\Gamma}$-$\bar{M}$ direction, the surface state near the Fermi

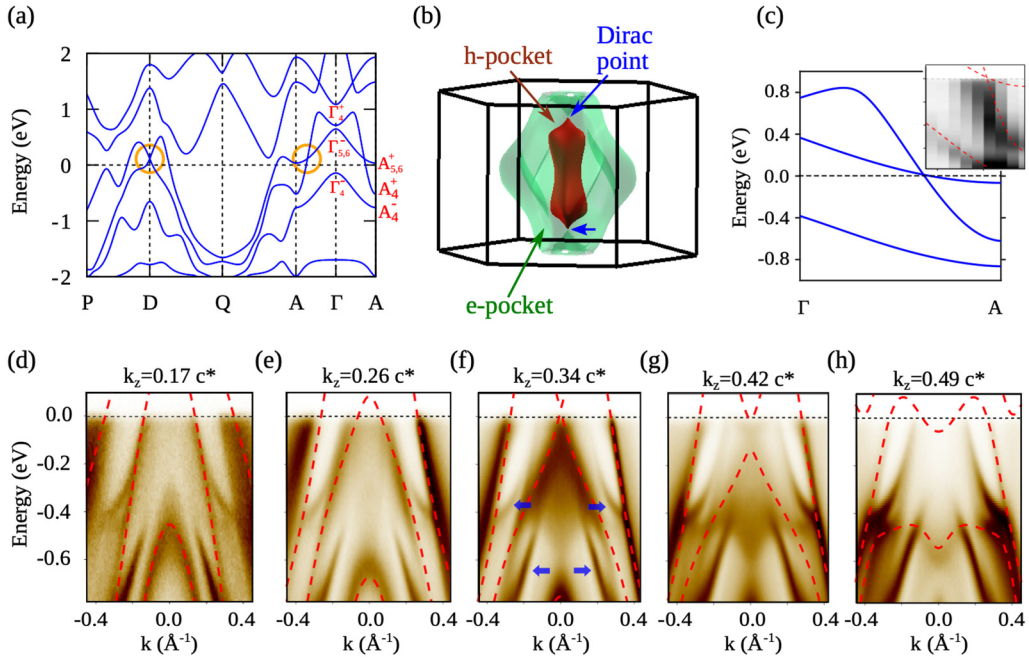

FIG. 2. (a) Band structure of $NiTe_2$ (including SOC) clearly showing the tilted type-II Dirac node along the Γ-*A* direction (at D). The irreducible representation of the bands (close to the Fermi energy) at the Γ and *A* points are also marked. (b) The Fermi surface of $NiTe_2$ originating from the crossing Dirac bands. The type-II Dirac points appear at the touching points of the electron and hole pockets. (c) The zoom of the band structure in the vicinity of the type-II Dirac point. The inset shows the experimental k_z dispersion along Γ-*A* deduced from the $h\nu$-dependent data measured along the $\bar{\Gamma}$-$\bar{K}$ direction [shown in part in (d)–(h)]. Note that the low velocity band of the Dirac node is not clearly resolved in our experiments (see text for details). (d)–(h) The measured band dispersion along the $\bar{K}$-$\bar{\Gamma}$-$\bar{K}$ direction for different k_z values, with the red dashed lines indicating the bulk DFT band structure. The blue arrows in panel (f) mark the surface states. Data were taken at photon energies of 17, 19, 21, 23, and 25 eV, respectively. Panel (f) corresponding to $k_z = 0.34\,c^*$ is closest to the location of the Dirac point ($k_z = 0.35\,c^*$ in our DFT calculations). Note that, for matching with the experimental data, we have shifted the DFT band structure downward by 100 meV.

energy has its origin from a band inversion above the Fermi energy (see Fig. 3(b), and Fig. S3 in SM [46]) and the corresponding surface Dirac cone lies above the Fermi level. While its Dirac-like nature is significantly altered far away from the $\bar{\Gamma}$ point, we demonstrate its topological origin by displaying its chiral spin texture in Fig. 4. Similar surface states have also been observed in other Te-based TMDs like $PtTe_2$ and $PdTe_2$, while they are absent in the Se based compounds like $PtSe_2$. This is a consequence of the avoided band inversion in $PtSe_2$ resulting from the reduced interlayer hopping [32,49].

IV. SPIN-POLARIZED SURFACE STATES

Since these surface states have a topological origin, we now focus on the spin polarization of the bands using spin-polarized ARPES. In Fig. 4(a) we display the spin-resolved data superimposed directly onto the spin-integrated band structure shown earlier in Figs. 3(c) and 3(d). The measured spin polarization matches reasonably well with the calculated spin textures reported in Figs. 4(b) and 4(g). In the present dataset, the spin component is always perpendicular to the dispersion direction. The most prominent feature in Figs. 4(a) and 4(b) is the crossover of two opposite spin polarizations of almost equal magnitude for the surface state bands crossing at the Γ point at a binding energy of ~ -1.4 eV. This confirms the helical nature of the spin-momentum locking in the vicinity of the surface Dirac point, resulting from the IBG with the $Z_2 = 1$ topological order. In Figs. 4(c)–4(e), we display the spin-polarized spectra and the spin polarization for the points marked by black arrows in Fig. 4(a). The measured polarization perpendicular to $\bar{\Gamma}$-$\bar{K}$ reaches almost 50%.

In the case of the bands along the $\bar{M}$-$\bar{\Gamma}$-$\bar{M}$ direction of the surface BZ [Figs. 4(f) and 4(g)], the polarization was measured for the electron-pocket-like surface states close to the Fermi energy. As discussed previously, although their shape is considerably different than usual topological surface states, the clear spin polarization demonstrates their topological origin (see Fig. S3 of SM [46]). These indeed appear to be the most prominent spin-polarized features also in the calculated spin polarization perpendicular to the $\bar{\Gamma}$-$\bar{M}$ direction. The high values of the measured and calculated spin polarization indicates that $NiTe_2$ belongs to the recently identified topological-ladder family of Pt/PdTe2 [33,48].

V. CONCLUSION

To summarize, we demonstrate $NiTe_2$ to be a type-II DSM using DFT-based *ab initio* calculations and explore its bulk and spin-polarized surface states using spin-resolved ARPES

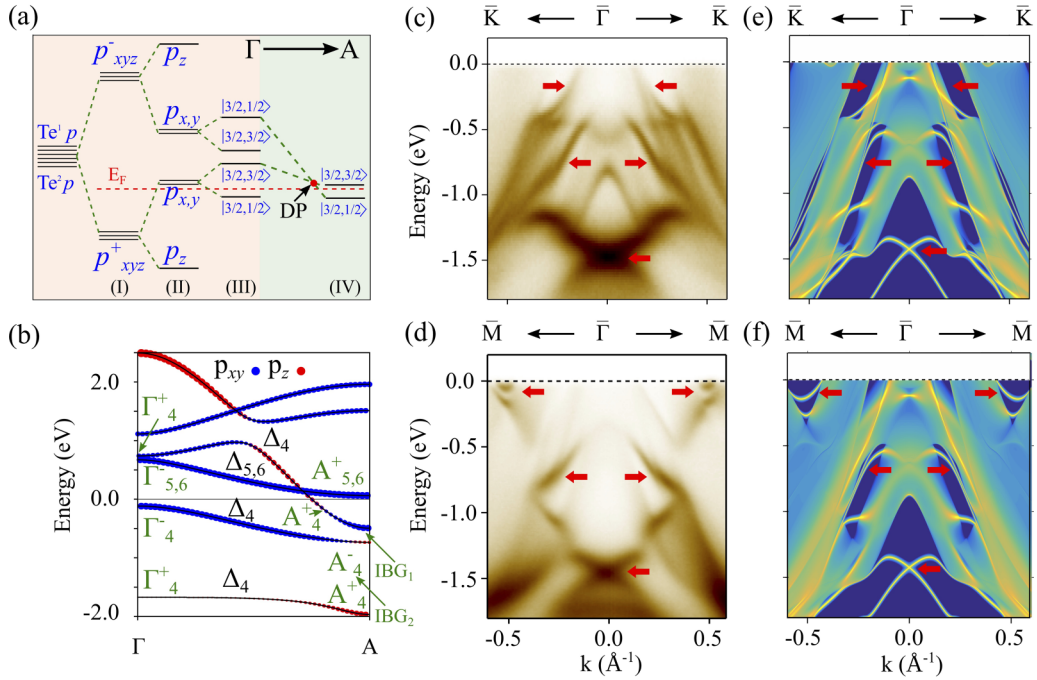

FIG. 3. (a) The evolution of the Te $5p$ orbitals in the formation of Dirac-cone states in $NiTe_2$. Step (I) shows the creation of bonding and antibonding orbitals. Step (II) shows the effect of the strong trigonal crystal field which separates the p_z orbitals from the $p_{x,y}$ orbitals. In step (III), we show the splitting of these states into the $|J, |m_J|\rangle$ states in the presence of SOC. In step (IV), we demonstrate the effect of out of plane dispersion and the formation of the Dirac point. (b) The orbital-resolved band structure and various band inversions along the ΓA high-symmetry direction are shown along with the irreducible representations of the bands. In panels (c) and (d) we show the ARPES data (for $h\nu = 24$ eV) along $\bar{K}$-$\bar{\Gamma}$-$\bar{K}$ and $\bar{M}$-$\bar{\Gamma}$-$\bar{M}$ (for $h\nu = 30$ eV) directions of the (001) surface BZ, respectively. ARPES results are consistent with the DFT predictions in panels (e) and (f). To match the ARPES results with DFT, we have used a surface potential of -0.14 eV.

measurements. We show that, in contrast to a similar class of materials like $PtTe_2$, $PdTe_2$, and $PtSe_2$, where the Dirac point is buried deep in the valence band, the Dirac point in $NiTe_2$ is located in the vicinity of the Fermi energy. In addition to the bulk Dirac node, the Te p-orbital manifold in $NiTe_2$ also gives rise to a series of IBGs with nontrivial Z_2 topological orders. Together, these give rise to topological Dirac nodes in the surface states characterized by the particular spin texture over a wide range of energies. Our findings establish $NiTe_2$ as a prime candidate for exploration of Dirac fermiology and applications in TMD-based spintronic devices, infrared plasmonics, and ultrafast optoelectronics.

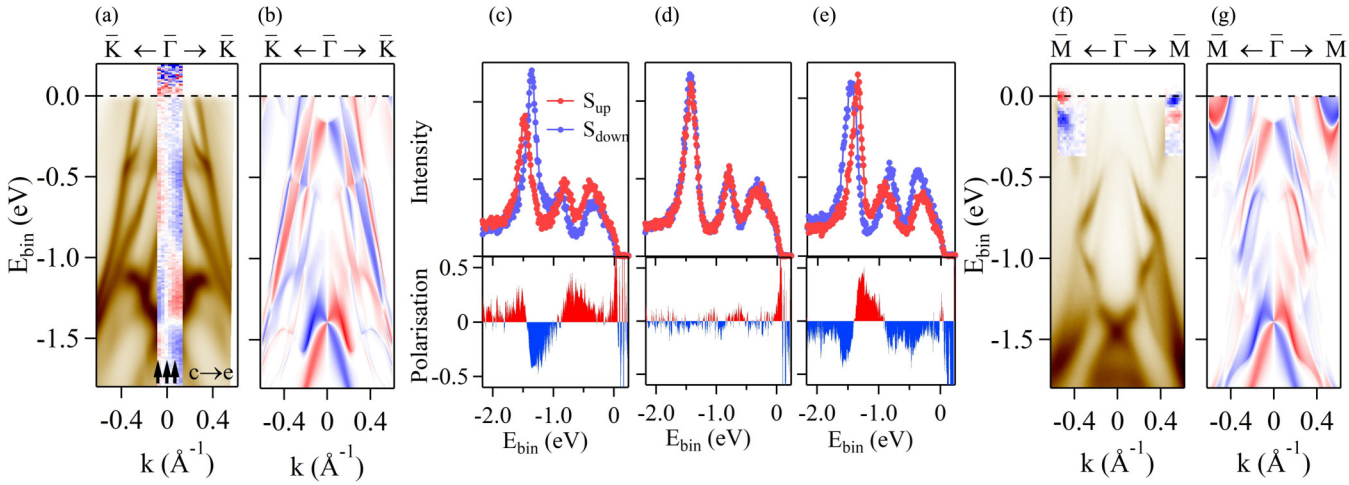

FIG. 4. Measured and calculated spin texture for the bands along $\bar{\Gamma}$-$\bar{K}$ (a),(b) and $\bar{\Gamma}$-$\bar{M}$ (f),(g) in the BZ. Experiments were performed in the same conditions as in Fig. 3; (c)–(e) spin-polarized spectra and spin polarization for the points along $\bar{\Gamma}$-$\bar{K}$ marked by black arrows in (a); in all figures red/blue indicate positive/negative polarization perpendicular to the high-symmetry direction. E_{bin} denotes the binding energy.

ACKNOWLEDGMENTS

A.A. acknowledges funding support by Science education and research board (SERB) and Department of Science and Technology (DST), Government of India. B.G. acknowledges CSIR for a senior research fellowship. A.A. and B.G. acknowledge HPC- IIT Kanpur for its computational facilities. This work has been partly performed in the framework of the nanoscience foundry and fine analysis (NFFA-MIUR Italy, Progetti Internazionali) facility.

B.G. and D.M. contributed equally to this work.

[1] A. Bansil, H. Lin, and T. Das, *Colloquium*: Topological band theory, Rev. Mod. Phys. **88**, 021004 (2016).

[2] N. P. Armitage, E. J. Mele, and A. Vishwanath, Weyl and dirac semimetals in three-dimensional solids, Rev. Mod. Phys. **90**, 015001 (2018).

[3] D. Kong and Yi Cui, Opportunities in chemistry and materials science for topological insulators and their nanostructures, Nat. Chem. **3**, 845 (2011).

[4] Z. Liu, W. Feng, H. Xin, Y. Gao, P. Liu, Y. Yao, H. Weng, and J. Zhao, Two-dimensional spin-valley-coupled dirac semimetals in functionalized sbas monolayers, Mater. Horiz. **6**, 781 (2019).

[5] F. Macedonio, A. Politano, E. Drioli, and A. Gugliuzza, Bi_2Se_3-assisted membrane crystallization, Mater. Horiz. **5**, 912 (2018).

[6] B. Bradlyn, J. Cano, Z. Wang, M. G. Vergniory, C. Felser, R. J. Cava, and B. A. Bernevig, Beyond dirac and weyl fermions: Unconventional quasiparticles in conventional crystals, Science **353**, 6299 (2016).

[7] Su-Yang Xu, I. Belopolski, N. Alidoust, M. Neupane, G. Bian, C. Zhang, R. Sankar, G. Chang, Z. Yuan, C.-C. Lee, S.-M. Huang, H. Zheng, J. Ma, D. S. Sanchez, B. Wang, A. Bansil, F. Chou, P. P. Shibayev, H. Lin, S. Jia, and M. Z. Hasan, Discovery of a weyl fermion semimetal and topological fermi arcs, Science **349**, 613 (2015).

[8] S.-M. Huang, Su-Yang Xu, I. Belopolski, C.-C. Lee, G. Chang, B. Wang, N. Alidoust, G. Bian, M. Neupane, C. Zhang, S. Jia, A. Bansil, H. Lin, and M. Z. Hasan, A weyl fermion semimetal with surface fermi arcs in the transition metal monopnictide TaAs class, Nat. Commun. **6**, 7373 (2015).

[9] B. Q. Lv, H. M. Weng, B. B. Fu, X. P. Wang, H. Miao, J. Ma, P. Richard, X. C. Huang, L. X. Zhao, G. F. Chen, Z. Fang, X. Dai, T. Qian, and H. Ding, Experimental Discovery of Weyl Semimetal TaAs, Phys. Rev. X **5**, 031013 (2015).

[10] Su-Yang Xu, N. Alidoust, I. Belopolski, Z. Yuan, G. Bian, T.-R. Chang, H. Zheng, V. N. Strocov, D. S. Sanchez, G. Chang, C. Zhang, D. Mou, Y. Wu, L. Huang, C.-C. Lee, S.-M. Huang, BaoKai Wang, A. Bansil, H.-T. Jeng, T. Neupert, A. Kaminski, H. Lin, S. Jia, and M. Zahid Hasan, Discovery of a weyl fermion state with fermi arcs in niobium arsenide, Nat. Phys. **11**, 748 (2015).

[11] C. Fang, M. J. Gilbert, X. Dai, and B. A. Bernevig, Multi-Weyl Topological Semimetals Stabilized by Point Group Symmetry, Phys. Rev. Lett. **108**, 266802 (2012).

[12] H. Weng, C. Fang, Z. Fang, B. A. Bernevig, and X. Dai, Weyl Semimetal Phase in Noncentrosymmetric Transition-Metal Monophosphides, Phys. Rev. X **5**, 011029 (2015).

[13] B. Singh, A. Sharma, H. Lin, M. Z. Hasan, R. Prasad, and A. Bansil, Topological electronic structure and weyl semimetal in the $TlBiSe_2$ class of semiconductors, Phys. Rev. B **86**, 115208 (2012).

[14] T.-R. Chang, S.-Y. Xu, D. S. Sanchez, W.-F. Tsai, S.-M. Huang, G. Chang, C.-H. Hsu, G. Bian, I. Belopolski, Z.-M. Yu, S. A. Yang, T. Neupert, H.-T. Jeng, H. Lin, and M. Z. Hasan, Type II Symmetry-Protected Topological Dirac Semimetals, Phys. Rev. Lett. **119**, 026404 (2017).

[15] Su-Yang Xu, N. Alidoust, G. Chang, H. Lu, B. Singh, I. Belopolski, D. S. Sanchez, X. Zhang, G. Bian, H. Zheng, M.-A. Husanu, Yi. Bian, S.-M. Huang, C.-H. Hsu, T.-R. Chang, H.-T. Jeng, A. Bansil, T. Neupert, V. N. Strocov, H. Lin, S. Jia, and M. Z. Hasan, Discovery of lorentz-violating type II weyl fermions in LaAlGe, Sci. Adv. **3**, e1603266 (2017).

[16] B. Q. Lv, Z. L. Feng, Q. N. Xu, X. Gao, J. Z. Ma, L. Y. Kong, P. Richard, Y. B. Huang, V. N. Strocov, C. Fang, H. M. Weng, Y. G. Shi, T. Qian, and H. Ding, Observation of three-component fermions in the topological semimetal molybdenum phosphide, Nature (London) **546**, 627 (2017).

[17] W. Gao, X. Zhu, F. Zheng, M. Wu, J. Zhang, C. Xi, P. Zhang, Y. Zhang, N. Hao, W. Ning *et al.*, A possible candidate for triply degenerate point fermions in trigonal layered $PtBi_2$, Nat. Commun. **9**, 3249 (2018).

[18] Z. Zhu, G. W. Winkler, Q. S. Wu, Ju Li, and A. A. Soluyanov, Triple Point Topological Metals, Phys. Rev. X **6**, 031003 (2016).

[19] J. Yu, B. Yan, and C.-X. Liu, Model hamiltonian and time reversal breaking topological phases of antiferromagnetic half-heusler materials, Phys. Rev. B **95**, 235158 (2017).

[20] I. C. Fulga and A. Stern, Triple point fermions in a minimal symmorphic model, Phys. Rev. B **95**, 241116(R) (2017).

[21] H. Yang, J. Yu, S. S. P. Parkin, C. Felser, C.-X. Liu, and B. Yan, Prediction of Triple Point Fermions in Simple Half-Heusler Topological Insulators, Phys. Rev. Lett. **119**, 136401 (2017).

[22] J. Wang, X. Sui, W. Shi, J. Pan, S. Zhang, F. Liu, Su-Huai Wei, Q. Yan, and B. Huang, Prediction of Ideal Topological Semimetals with Triply Degenerate Points in the $NaCu_3Te_2$ Family, Phys. Rev. Lett. **119**, 256402 (2017).

[23] S. M. Young, S. Zaheer, J. C. Y. Teo, C. L. Kane, E. J. Mele, and A. M. Rappe, Dirac Semimetal in Three Dimensions, Phys. Rev. Lett. **108**, 140405 (2012).

[24] S. M. Young and C. L. Kane, Dirac Semimetals in Two Dimensions, Phys. Rev. Lett. **115**, 126803 (2015).

[25] B. J. Wieder, Y. Kim, A. M. Rappe, and C. L. Kane, Double Dirac Semimetals in Three Dimensions, Phys. Rev. Lett. **116**, 186402 (2016).

[26] Z. K. Liu, B. Zhou, Y. Zhang, Z. J. Wang, H. M. Weng, D. Prabhakaran, S.-K. Mo, Z. X. Shen, Z. Fang, X. Dai, Z. Hussain, and Y. L. Chen, Discovery of a three-dimensional topological dirac semimetal, Na_3Bi, Science **343**, 864 (2014).

[27] Z. K. Liu, J. Jiang, B. Zhou, Z. J. Wang, Y. Zhang, H. M. Weng, D. Prabhakaran, S-K. Mo, H. Peng, P. Dudin, T. Kim, M. Hoesch, Z. Fang, X. Dai, Z. X. Shen, D. L. Feng, Z. Hussain, and Y. L. Chen, A stable three-dimensional topological dirac semimetal Cd_3As_2, Nat. Mater. **13**, 677 (2014).

[28] M. Neupane, Su-Yang Xu, R. Sankar, N. Alidoust, G. Bian, C. Liu, I. Belopolski, T.-R. Chang, H.-T. Jeng, H. Lin, A. Bansil, F. Chou, and M. Z. Hasan, Observation of a three-dimensional topological dirac semimetal phase in high-mobility Cd_3As_2, Nat. Commun. **5**, 3786 (2014).

[29] S. Borisenko, Q. Gibson, D. Evtushinsky, V. Zabolotnyy, B. Büchner, and R. J. Cava, Experimental Realization of a Three-Dimensional Dirac Semimetal, Phys. Rev. Lett. **113**, 027603 (2014).

[30] Z. Wang, Y. Sun, X.-Q. Chen, C. Franchini, G. Xu, H. Weng, Xi Dai, and Z. Fang, Dirac semimetal and topological phase transitions in A_3Bi (a = Na, K, Rb), Phys. Rev. B **85**, 195320 (2012).

[31] Z. Wang, H. Weng, Q. Wu, Xi Dai, and Z. Fang, Three-dimensional dirac semimetal and quantum transport in Cd_3As_2, Phys. Rev. B **88**, 125427 (2013).

[32] M. Yan, H. Huang, K. Zhang, E. Wang, W. Yao, Ke Deng, G. Wan, H. Zhang, M. Arita, H. Yang, Z. Sun, H. Yao, Y. Wu, S. Fan, W. Duan, and S. Zhou, Lorentz-violating type II dirac fermions in transition metal dichalcogenide $PtTe_2$, Nat. Commun. **8**, 257 (2017).

[33] M. S. Bahramy, O. J. Clark, B. J. Yang, J. Feng, L. Bawden, J. M. Riley, I. Marković, F. Mazzola, V. Sunko, D. Biswas, S. P. Cooil, M. Jorge, J. W. Wells, M. Leandersson, T. Balasubramanian, J. Fujii, I. Vobornik, J. E. Rault, T. K. Kim, M. Hoesch, K. Okawa, M. Asakawa, T. Sasagawa, T. Eknapakul, W. Meevasana, and P. D. C. King, Ubiquitous formation of bulk dirac cones and topological surface states from a single orbital manifold in transition-metal dichalcogenides, Nat. Mater. **17**, 21 (2017).

[34] A. Politano, G. Chiarello, B. Ghosh, K. Sadhukhan, C.-N. Kuo, C. S. Lue, V. Pellegrini, and A. Agarwal, 3d Dirac Plasmons in the Type II Dirac Semimetal $PtTe_2$, Phys. Rev. Lett. **121**, 086804 (2018).

[35] K. Zhang, M. Yan, H. Zhang, H. Huang, M. Arita, Z. Sun, W. Duan, Y. Wu, and S. Zhou, Experimental evidence for type II dirac semimetal in $PtSe_2$, Phys. Rev. B **96**, 125102 (2017).

[36] H.-J. Noh, J. Jeong, En-Jin Cho, K. Kim, B. I. Min, and B.-G. Park, Experimental Realization of Type II Dirac Fermions in a $PdTe_2$ Superconductor, Phys. Rev. Lett. **119**, 016401 (2017).

[37] F. Fei, X. Bo, R. Wang, B. Wu, J. Jiang, D. Fu, M. Gao, H. Zheng, Y. Chen, X. Wang, H. Bu, F. Song, X. Wan, B. Wang, and G. Wang, Nontrivial berry phase and type II dirac transport in the layered material $PdTe_2$, Phys. Rev. B **96**, 041201(R) (2017).

[38] C. Xu, B. Li, W. Jiao, W. Zhou, B. Qian, R. Sankar, N. D. Zhigadlo, Y. Qi, D. Qian, F.-C. Chou, and X. Xu, Topological type II dirac fermions approaching the fermi level in a transition metal dichalcogenide $NiTe_2$, Chem. Mater. **30**, 4823 (2018).

[39] E. Uchida and H. Kondoh, Magnetic properties of nickel telluride, J. Phys. Soc. Jpn. **11**, 21 (1956).

[40] M. Ettenberg, K. L. Komarek, and E. Miller, Thermodynamic properties of nickel-tellurium alloys, J. Solid State Chem. **1**, 583 (1970).

[41] G. Y. Guo and W. Y. Liang, Study of the electronic structures of ni-group metal ditellurides: $NiTe_2$, $PdTe_2$ and $PtTe_2$ by the self-consistent LMTO-ASA method, J. Phys. C **19**, 5365 (1986).

[42] P. J. Orders, J. Liesegang, R. C. G. Leckey, J. G. Jenkin, and J. D. Riley, Angle-resolved photoemission from the valence bands of $NiTe_2$, $PdTe_2$ and $PtTe_2$, J. Phys. F **12**, 2737 (1982).

[43] J. F. H. L. Monteiro, M. B. Marciniak, A. R. Jurelo, E. C. Siqueira, F. T. Dias, and J. L. P. Junior, Synthesis and microstructure of $NiTe_2$, J. Cryst. Growth **478**, 129 (2017).

[44] B. Zhao, W. Dang, Y. Liu, Bo Li, J. Li, J. Luo, Z. Zhang, R. Wu, H. Ma, G. Sun, Yu Huang, X. Duan, and X. Duan, Synthetic control of two-dimensional $NiTe_2$ single crystals with highly uniform thickness distributions, J. Am. Chem. Soc. **140**, 14217 (2018).

[45] Q. Liu, F. Fei, Bo Chen, X. Bo, B. Wei, S. Zhang, M. Zhang, F. Xie, M. Naveed, X. Wan, F. Song, and B. Wang, Nontopological origin of the planar hall effect in the type II dirac semimetal $NiTe_2$, Phys. Rev. B **99**, 155119 (2019).

[46] See Supplemental Material at http://link.aps.org/supplemental/10.1103/PhysRevB.100.195134 for details of (1) sample preparation and characterization, (2) computational details, (3) ARPES measurements, (4) topological band inversions, and (5) ARPES measurements with potassium doping (see, also, Refs. [50–57] therein).

[47] V. N. Strocov, Intrinsic accuracy in 3-dimensional photoemission band mapping, J. Electron Spectrosc. Relat. Phenom. **130**, 65 (2003).

[48] O. J. Clark, F. Mazzola, I. Marković, J. M. Riley, J. Feng, B.-J. Yang, K. Sumida, T. Okuda, J. Fujii, I. Vobornik, T. K. Kim, K. Okawa, T. Sasagawa, M. S. Bahramy, and P. D. C. King, A general route to form topologically-protected surface and bulk dirac fermions along high-symmetry lines, Electronic Structure **1**, 014002 (2019).

[49] O. J. Clark, M. J. Neat, K. Okawa, L. Bawden, I. Marković, F. Mazzola, J. Feng, V. Sunko, J. M. Riley, W. Meevasana, J. Fujii, I. Vobornik, T. K. Kim, M. Hoesch, T. Sasagawa, P. Wahl, M. S. Bahramy, and P. D. C. King, Fermiology and Superconductivity of Topological Surface States in $PdTe_2$, Phys. Rev. Lett. **120**, 156401 (2018).

[50] C. Bigi, P. K. Das, D. Benedetti, F. Salvador, D. Krizmancic, R. Sergo, A. Martin, G. Panaccione, G. Rossi, J. Fujii, and I. Vobornik, Very efficient spin polarization analysis (VESPA): new exchange scattering-based setup for spin-resolved ARPES at APE-NFFA beamline at Elettra, J. Synchrotron Radiat. **24**, 750 (2017).

[51] G. Panaccione, I. Vobornik, J. Fujii, D. Krizmancic, E. Annese, L. Giovanelli, F. Maccherozzi, F. Salvador, A. De Luisa, D. Benedetti, A. Gruden, P. Bertoch, F. Polack, D. Cocco, G. Sostero, B. Diviacco, M. Hochstrasser, U. Maier, D. Pescia, C. H. Back, T. Greber, J. Osterwalder, M. Galaktionov, M. Sancrotti, and G. Rossi, Advanced photoelectric effect experiment beamline at elettra: A surface science laboratory coupled with synchrotron radiation, Rev. Sci. Instrum. **80**, 043105 (2009).

[52] W. Kohn and L. J. Sham, Self-consistent equations including exchange and correlation effects, Phys. Rev. **140**, A1133 (1965).

[53] G. Kresse and D. Joubert, From ultrasoft pseudopotentials to the projector augmented-wave method, Phys. Rev. B **59**, 1758 (1999).

[54] G. Kresse and J. Furthmüller, Efficient iterative schemes for ab initio total-energy calculations using a plane-wave basis set, Phys. Rev. B **54**, 11169 (1996).

[55] J. P. Perdew, K. Burke, and M. Ernzerhof, Generalized Gradient Approximation Made Simple, Phys. Rev. Lett. **77**, 3865 (1996).

[56] N. Marzari and D. Vanderbilt, Maximally localized generalized wannier functions for composite energy bands, Phys. Rev. B **56**, 12847 (1997).

[57] Q. Wu, S. Zhang, H.-F. Song, M. Troyer, and A. A. Soluyanov, WannierTools: An open-source software package for novel topological materials, Comput. Phys. Commun. **224**, 405 (2018).